ARTICLE

Chinese Journal of Structural Chemistry

# $CeO_2$ Particles Anchored to $Ni_2P$ Nanoplate for Efficient Photocatalytic Hydrogen Evolution

Teng Yan[1], Xiaojie Zhang[2], Hua Liu[1]* and Zhiliang Jin[1]*

[1]*School of Chemistry and Chemical Engineering, Ningxia Key Laboratory of Solar Chemical Conversion Technology, Key Laboratory for Chemical Engineering and Technology, State Ethnic Affairs Commission, North Minzu University, Yinchuan 750021, China*

[2]*Department of Metallurgical and Chemical Engineering, Jiyuan Vocational and Technical College, Jiyuan 459000, China*

**ABSTRACT** Photocatalytic hydrogen evolution can convert intermittent and dispersive solar energy into hydrogen with high energy density, which is expected to fundamentally solve the problems of environmental pollution and energy shortages. In this experiment, the performance of the catalyst is modified by introducing cocatalyst and morphology control. $Ni(OH)_2$ nanoflowers are used as substrates to derive nanoplate stack $Ni_2P$ by high-temperature phosphating method, and a great many of $CeO_2$ nanoparticles are anchored in the $Ni_2P$. This unique 3D/0D combination effectively inhibits the agglomeration of $CeO_2$ nanoparticles and shortens the electron transfer path. Secondly, the introduction of metal-like performance of $Ni_2P$ broadens the light absorption range of the catalyst and reduces the overpotential of the catalyst, which is a key factor in enhancing the catalytic activity. The design ideas of this experiment have reference significance for the design of efficient and environmentally friendly photocatalysts.

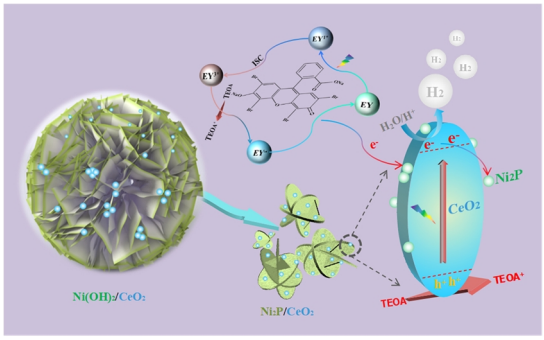


**Keywords:** $CeO_2$, $Ni_2P$, photocatalysis, hydrogen evolution

## n INTRODUNTION

In recent years, semiconductor photocatalysts have received widespread attention for hydrogen evolution from water splitting. This technology is expected to solve the conflict between environment and energy.[1-4] However, a single photocatalyst often has the disadvantages such as low photoadsorption, and high carrier recombination, which will affect the hydrogen evolution performance of the catalyst.[5-8] In terms of promoting the separation of photogenerated carriers, the noble metal (Ag, Pt) with higher work function has excellent performance, but their scarcity and high cost make it impossible to commercialize precious metals.[9,10] Therefore, it has important practical significance to prepare a stable and efficient catalyst with suitable cost.[11-14]

Hitherto, a large number of catalysts based on transition metal sulfides,[15-19] transition metal phosphides (TMPs),[20] transition metal carbides,[21-23] transition metal oxides[24,25] and nickel-based catalysts[26,27] have been reported. Among nickel-based catalysts, $Ni(OH)_2$ has good electrochemical performance and unique light absorption characteristics, but its poor electron mobility has led to relatively few reports in the field of photocatalysis. Researches demonstrated that the difference in the microstructure of the catalyst will affect the number of active sites, which in turn affects the hydrogen evolution activity,[28,29] Cao et al.[26] used an electrostatic method to synthesize a 2D/3D $Ni(OH)_2$/g-$C_3N_4$ composite catalyst to construct a Z-scheme heterojunction, and this catalyst has better hydrogen evolution performance than Pt/g-$C_3N_4$. In contrast, TMPs materials represented by NiP, $Ni_2P$ and $Ni_5P_4$ have been extensively studied due to their metal-like properties and excellent light absorption properties. The P atom has good electronegativity, so the performance of the catalyst with high P content is relatively better. Wen et al.[30] synthesized a $Ni_2P$-g-$C_3N_4$ (in situ) composite catalyst by a one-step co-heating solution method. The apparent quantum efficiency at 420 nm is as high as 18%. Shi et al.[31] used $Ni_2P$ as a co-catalyst to modify the p–n heterojunction, and the hydrogen evolution rate of NiO/$Ni_2P$/CN reached 5.04 μmol/h. However, most of the nickel phosphide reported in the literature is nanoparticles.

As a common rare earth oxide, cerium dioxide ($CeO_2$) has been used in the field of solar cells and hydrogen evolution by virtue of suitable band gap and rich redox properties.[32] Studies have shown that the different crystal faces of $CeO_2$ play different roles in photocatalysis. The photo-generated carrier mobility of the (111) and (100) faces is different. Among them, the (100) faces have more adsorbed hydroxyl groups and oxygen vacancies, which are the main accumulation areas of holes, and the electron is transferred to the (111) surface.[33-35] Taking advantage of $CeO_2$, many $CeO_2$-based composite materials (CdSe/$CeO_2$,[36] $CeO_2$@α-$Fe_2O_3$[37]) have played a huge role in photocatalytic hydrogen evolution and pollutant degradation. Zou et al. used the interfacial effect of $CeO_2$ to hybridize g-$C_3N_4$ composite material so as to make the hydrogen production of the composite catalyst reach 430 μmol/g in 5 h.[38]

In this paper, high temperature phosphating method is used to convert $Ni(OH)_2$ into $Ni_2P$, and the effect of $CeO_2$ on the performance of the two catalysts is studied in detail from the perspective of band structure and morphology combination. $CeO_2$ nanoparticles are embedded in the structures of nanoflowers, which significantly improves the interface charge transfer efficiency and remarkably improves the hydrogen production activity of NCP-15.

## n RESULTS AND DISCUSSION

  
DOI: 10.14102/j.cnki.0254-5861.2021-0057

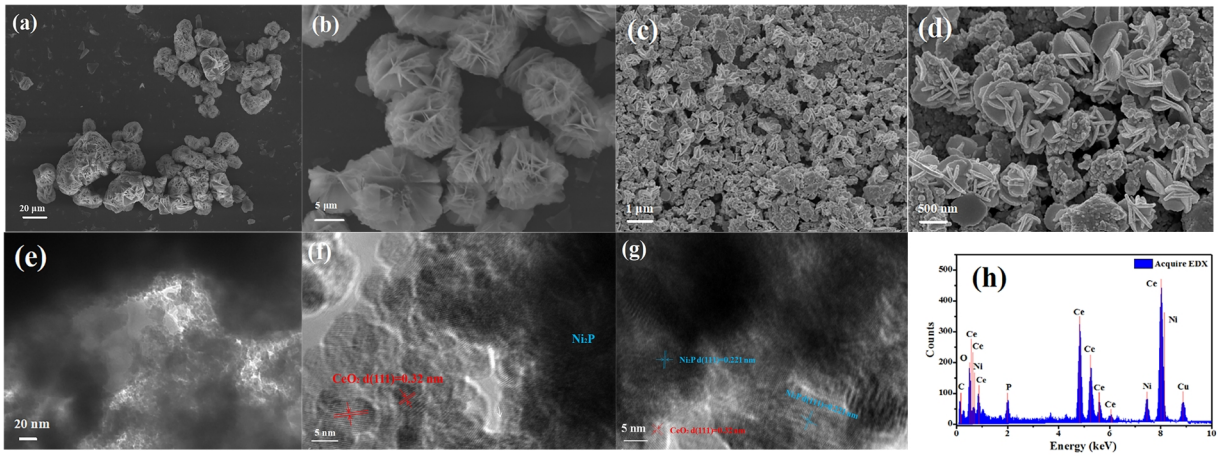


**Figure 1.** SEM images of (a, b) $Ni(OH)_2$ and (c, d) $Ni_2P$. (e–g) HRTEM images and (h) EDX of NPC-15.

**XRD Analysis.** The crystal structures and phase compositions of $Ni(OH)_2$, $Ni_2P$, $CeO_2$, NHC-15 and NPC-x were characterized by powder XRD. In Figure S1a, the main diffraction peaks of $Ni(OH)_2$ are located at 19.17°, 33.25°, 38.62°, 52.08° and 59.4°, corresponding to the (001), (100), (214), (102) and (110) planes of $Ni(OH)_2$ (PDF#14-117). Specifically, characteristic peaks of $Ni_2P$ are observed at 40.8°, 44.64°, 47.4° and 54.33°, which can be ascribed to the (111), (201), (210) and (002) planes, respectively, indicating that the calcined phosphating can produce highly crystalline $Ni_2P$. For $CeO_2$, the typical diffraction peaks at $2\theta$ = 28.67°, 33.14°, 47.74° and 56.64° correspond to the crystal planes of (111), (200), (220), and (311) in the PDF#1-800. With respect to NPC-x, the typical diffraction peaks of $Ni_2P$ and $CeO_2$ can be clearly observed, and the peaks of $Ni_2P$ gradually weaken with increasing the content of $Ce_2O$, indicating that the preparation of NPC-x was successful. Similarly, NHC-15 also has no extraneous diffraction peaks.

**Morphology and Structure.** The morphologies of pristine $Ni_2P$, $Ni(OH)_2$ and microstructures of $CeO_2$, NPC-15 were characterized by SEM and HR-TEM, respectively. From Figure 1a, pure $Ni(OH)_2$ has a carnation-like morphology with a main diameter of 8–20 μm. In Figure 1b, the average thickness of $Ni(OH)_2$ petals is about 130 nm, and the unique interface structure of nanoflowers facilitates the anchoring of reactants and product molecules. In Figure 1c, d, $Ni_2P$ showed a regular flower-like structure and a small amount of agglomerated large particles, and the average thickness of the petals was reduced to 40 nm. Under high-temperature calcinations, the carnation structure changes and shrinks, resulting in a corresponding reduction in the size and thickness of $Ni_2P$. Uniform size and controllable morphology are two essential factors for efficient catalysts. The 0D $CeO_2$ quantum dot structure was observed in the middle part of Figure 1e. The HRTEM image, as shown in Figure 1g, f, obviously reveals the close interface contact between $CeO_2$ and $Ni_2P$. The lattice spacing of the two groups is 0.32 and 0.221 nm which are assigned to the distance between the $CeO_2$ (111) and $Ni_2P$ (111) crystal planes, respectively. As shown in Figure 1h, the energy dispersive X-ray (EDX) spectroscopy further demonstrates the existence of Ce, O, Ni and P elements in the NPC-15 sample.

**XPS Analysis.** The chemical compositions of surface components of catalysts were studied by XPS[39] expounding the interaction between $Ni(OH)_2$, $Ni_2P$ and $CeO_2$. In Figure 2a, b, the necessary elements including Ni, P, Ce, O and C have been detected, indicating that the preparation of all photocatalysts is successful. In Figure 2c, the peaks at 856.3 and 862.15 eV correspond to Ni $2p_{3/2}$, and other peaks at 874 and 880.04 eV can

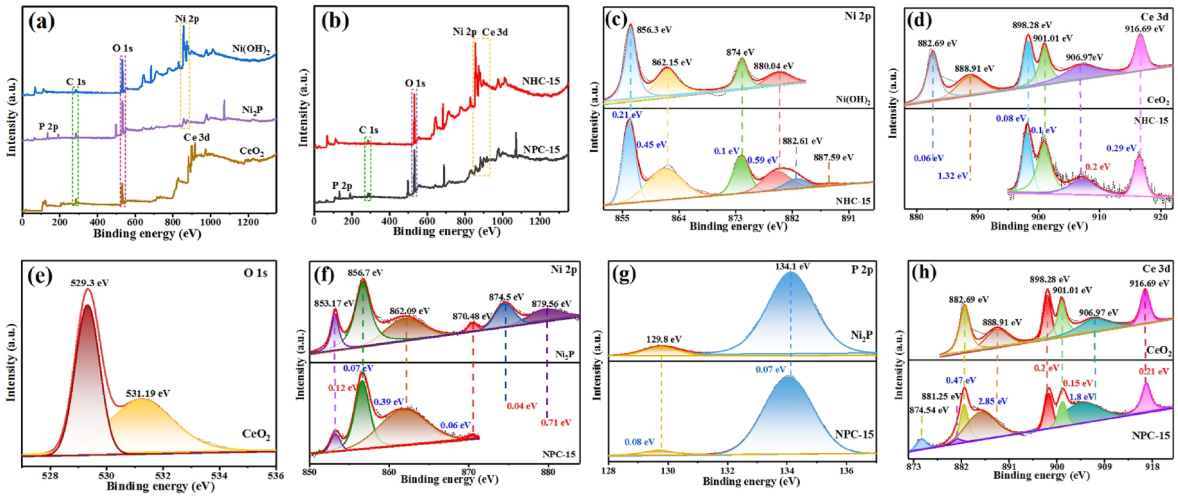


**Figure 2.** (a, e) XPS spectra of $Ni_2P$, $Ni(OH)_2$, $CeO_2$, NHC-15 and NPC-15. High-resolution (b, f) Ni 2*p*, (c, h) Ce 3*d*, and (d, i) O 1*s* of the samples.

  
DOI: 10.14102/j.cnki.0254-5861.2021-0057

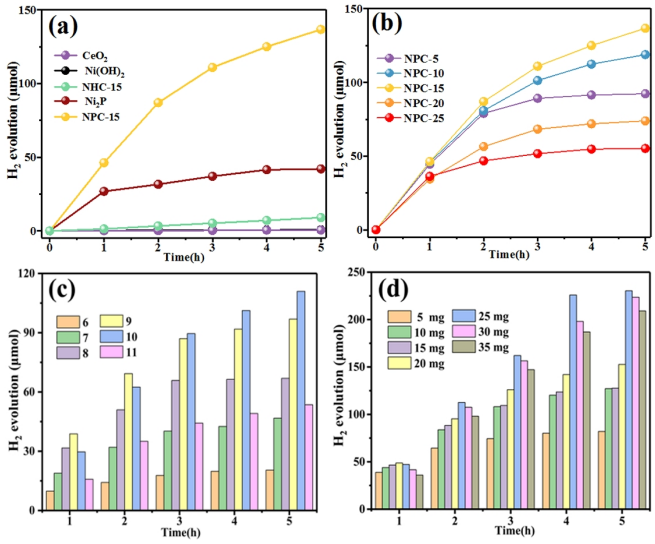


**Figure 3.** Photocatalytic activity of (a) $Ni_2P$, $Ni(OH)_2$, $CeO_2$, NHC-15 (b) NPC-x. (c, d) $H_2$ evolution of NPC-15 at different amounts of EY and different pH values.

be allocated to the Ni $2p_{1/2}$.[40] In Fig. 3d, h, the peaks at 882.69, 888.91 and 898.28 eV refer to $Ce^{4+}$ $3d_{3/2}$, while the peaks at 901.01, 906.97 and 916.69 eV refer to $Ce^{4+}$ $3d_{5/2}$.[41] The two spectra of O 1*s* in $CeO_2$ presented in Figure 2e show peaks at 529.3 and 531.19 eV, corresponding to the Ce–O and adsorbed oxygen and $H_2O$, respectively.[41] Figure 2f shows the XPS spectrum of Ni 2*p* for pure $Ni_2P$. The peaks at 853.17 and 870.48 eV are related to $Ni^{\delta+}$ ($0<\delta<2$) in $Ni_2P$, and those strong at 856.7 and 874.5 are both attributed to the oxidized Ni species ($Ni^{2+}$).[42] Furthermore, two distinguishable signals at 862.09 and 879.56 eV correspond to the satellite peaks of Ni $2p_{3/2}$ and $2p_{1/2}$ peaks, respectively.[43] In the P 2*p* spectra (Figure 2f), two salient peaks at 129.8 and 134.1 eV can be attributed to the $P^{\delta-}$ in $Ni_2P$ and nickel phosphate formed on the surface of catalyst in air contact.[43] The characteristic peaks of the composite catalysts NHC-15 and NPC-15 are blue- and red-shifted, revealing not only simple physical adsorption but also electron transfer between different types of catalysts.

**Photocatalytic Hydrogen Evolution Performance.** As shown in Figure 3a, $CeO_2$ and $Ni(OH)_2$ have almost no hydrogen evolution activity. EY provides $Ni_2P$ with a large number of electrons in the dye-sensitized system, and the amount of hydrogen produced of $Ni_2P$ reached 42 μmol. In addition, the test results show that EY/TEOA/water has no hydrogen production activity. For the composite catalyst NPC-x, $Ni_2P$ still maintains a flower-like structure formed by flaky polymerization after phosphating, which helps load small $CeO_2$ particles. Therefore, the hydrogen evolution volume of NPC-15 is as high as 145 μmol, which is more than four times that of $Ni_2P$. Less $CeO_2$ cannot fully couple with $Ni_2P$, so the hydrogen production activity is low; excess $CeO_2$ nanoparticles are prone to agglomeration and cannot be in close contact with $Ni_2P$. The improved catalytic performance of NHC-15 is due to the combination of morphology and interlaced energy band position. The flower-like structure is conducive to the anchoring of $CeO_2$ nanoparticles. Besides, the staggered energy band structure of the two catalysts can enhance the separation efficiency of photogenerated carriers.

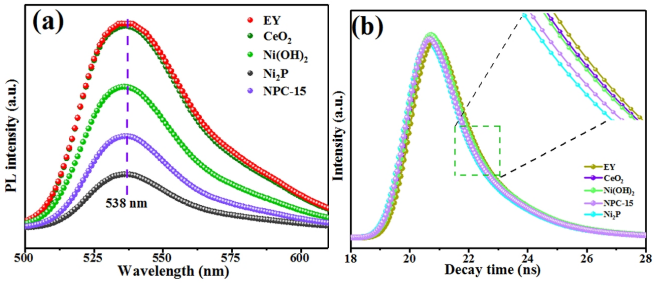


**Figure 4.** (a) PL and (b) TRPL spectra of EY, $CeO_2$, $Ni(OH)_2$, $Ni_2P$, and NPC-15.

The pH value and EY quality of the solution have a significant impact on the hydrogen production test of the catalyst. In Figure 3c, the NPC-15 has good hydrogen evolution activity in solution at pH 10. The high $H^+$ concentration in the sacrificial reagent leads to the protonation of TEOA, and the low H concentration weakens the thermodynamic driving force. As shown in Figure 3d, the amount of hydrogen evolution of NPC-15 was 230 μmol. EY acts as an electron donor in the catalytic system. The reduction of EY mass not only reduces the number of electrons participating in the reduction reaction, but also reduces the absorbance of the catalyst;[44] excessive EY will agglomerate and disperse into the solution and will not participate in the hydrogen evolution reaction.[45] Free EY molecules can absorb part of the visible light, thus reducing the number of injected photons.[46,47]

**BET Surface Areas and Pore Size Distributions.** Figure S2a–d shows the pore size and specific surface areas distribution of three pristine samples and the composites. According to the classification of the International Union of Pure and Applied Chemistry (IUPAC), all samples tested show H3 hysteresis loops and type IV isotherms, indicating that the catalytic material has mesoporous properties. The $S_{BET}$ of $Ni(OH)_2$ is 10.75 $m^2g^{-1}$, and the thin-layer flower-like $Ni(OH)_2$ undergoes condensation and agglomeration after high temperature phosphating to form plate-like $Ni_2P$. In Table S1, the specific surface area of $Ni_2P$ is 5.67 $m^2g^{-1}$, which is associated with changes in the microstructure of the material. The BET surface area of $CeO_2$ nanoparticles is as high as 91.47 $m^2g^{-1}$. Moreover, the pore volume and specific surface area of NPC-15 are significantly reduced, which may be related to a large number of $CeO_2$ nanoparticles occupying the surface area of $Ni_2P$. The analysis shows that the enhanced hydrogen evolution performance of NPC-15 is mostly ascribed to the increase in the separation efficiency of electron and holes, rather than the change in specific surface area.

**Optical Properties of the Photocatalysts.** Figure S3a, b exhibits the UV-vis absorbance spectra of $CeO_2$, $Ni(OH)_2$, $Ni_2P$ and NPC-x. The spectrum of CdS is significantly different from that of the traditional semiconductor catalysts, with three distinct absorption bands falling in the 250–800 nm range. The wide absorption band of 250–300 nm can confirm the charge transfer from O 2*p* orbital to the Ni 3*d* of $Ni^{2+}$ ions. The absorption band at 300–800 nm is caused by the *d*–*d* transition of $Ni^{2+}$ in the octahedron. Black $Ni_2P$ has high adsorption in the 250–800 nm range. Compared with $CeO_2$, the optical absorbance of the NPC-x in the region of 380–800 nm has been greatly improved. Besides, the

  
DOI: 10.14102/j.cnki.0254-5861.2021-0057

**Table 1.** Lifetimes of EY, $Ce_2O$, $Ni(OH)_2$, NPC-15, and $Ni_2P$

| Samples | $\tau_1$ [ns] | $\tau_2$ [ns] | $\tau_{ave}$ [ns] |
|---|---|---|---|
| EY | 1.04 (85.67%) | 1.99 (14.33%) | 1.11 |
| $Ce_2O$ | 1.08 (90.49%) | 2.18 (9.51%) | 1.14 |
| $Ni(OH)_2$ | 0.99 (73.58%) | 1.80 (26.42%) | 1.12 |
| NPC-15 | 1.01 (79.65%) | 1.84 (20.35%) | 1.11 |
| $Ni_2P$ | 0.96 (73.04%) | 1.73 (26.96%) | 1.09 |

light absorption intensity of the NPC-x gradually decreases with the increase of $CeO_2$ content, which proves that the $CeO_2$ loading on $Ni_2P$ is successful. Figure S3c, d shows the band gaps of $Ni(OH)_2$ and $CeO_2$ are calculated using the Kubelka-Munk equation, in which n is related to the properties of the semiconductor, and the direct and indirect band gaps are respectively 1 and 4.[48] The $E_g$ values of $Ni(OH)_2$ and $CeO_2$ are determined to be 2.31 and 2.59 eV, respectively.

**PL Experiments.** The PL spectra of the catalyst were tested at excitation wavelength 480 nm. The semiconductor material absorbs photons. The ground state electrons are excited to transition to the conduction, and then return to the ground state irradiative decay process. In Figure 4a, the higher PL peak means that the photo-generated carriers will be easily transferred to the surface. EY shows that the high intensity emission peak centered at 538 nm is caused by the severe recombination of photo-generated carriers. Compared with $CeO_2$ and $Ni(OH)_2$, the PL signal intensity of the composite catalyst NPC-15 is significantly reduced, indicating that $Ni_2P$ can efficiently capture electrons on $CeO_2$. Moreover, TRPL spectroscopy (Figure 4b) was used to study the catalyst charge transfer dynamics. According to the kinetic function principle, the curve for decay can be fitted: $I(t) = A_1\exp(-t/\tau_1) + A_2\exp(-t/\tau_2)$, where A and t represent the corresponding percentages and lifetime, respectively.[49] In addition, the average lifetime ($\tau_{ave}$) of photocarrier recombination can be calculated by $\tau_{ave} = (A_1\tau_1^2 + A_2\tau_2^2)/(A_1\tau_1 + A_2\tau_2)$. The decrease in the average lifetime of NCP-15 indicates that $CeO_2$ quantum dots transfer electrons to $Ni_2P$ in a non-radiative quenching manner.[50] The low emission peak intensity and short average life of $Ni_2P$ prove its excellent performance.

**Electrochemical Analysis.** Figure S4a records the transient photocurrent responses of the catalyst on the FTO glass after four on-off illumination cycles. Generally, the photocurrent response is formed by the diffusion of charge carriers separated from the inner to the free charge acceptors in the electrolyte or on the surface of the catalyst. $CeO_2$ and $Ni(OH)_2$ exhibit low photocurrent intensity, while $Ni_2P$ and NPC-15 have stable reversible and good reproducibility, indicating that charge carriers have good separation effects. Firstly, $Ni_2P$ and NPC-x have stronger photo-absorption ability and can generate more photo-induced carriers; secondly, $Ni_2P$ acts as an electron trap to trap electrons before the photo-generated carriers recombine. Electrochemical impedance spectroscopy (EIS) is a powerful tool for studying the electron transfer between the electrolyte solution and the catalyst on the working electrode.[51] In Figure S4b, NPC-15 exhibits semicircular arc, indicating a higher conductivity and lower electron transfer resistance.[52] Linear sweep voltammetry (LSV) curves are used to study the electrochemical hydrogen evolution activity of the catalyst. Compared with other

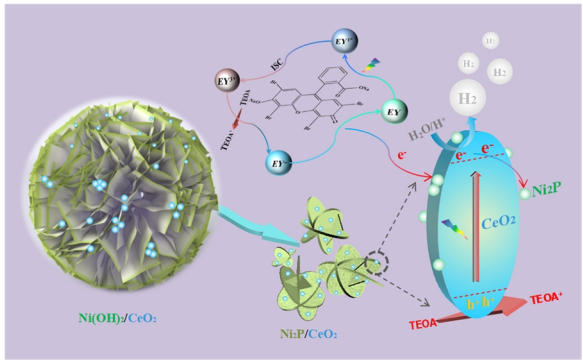


**Figure 5.** Photocatalytic hydrogen production reaction mechanism diagram of NHC-15 and NPC-15.

catalysts, the cathode current density and overpotential of NPC-15 and NPCO-15 are lower, which suggests that $Ni(OH)_2$ and $Ni_2P$ can effectively reduce the overpotential of the catalyst and promote the surface reduction reaction kinetics and proton reduction. The slopes of the catalysts in Figure S4d, e are positive, so they are n-type semiconductors. The flat band potentials ($E_{fb}$) of $Ni_2P$ and $CeO_2$ are –0.21 and –0.49 V, respectively. After conversion, the conduction band potentials ($E_{CB}$) relative to the saturated calomel electrodes (SCE) $Ni_2P$ and $CeO_2$ are –0.41 and –0.69 V, respectively. Compared with the standard hydrogen electrode ($E_{NHE} = E_{SCE} + 0.24$ V), the $E_{CB}$ values of $Ni_2P$ and $CeO_2$ are –0.17 and –0.45 V, respectively. It is reported that the $E_{CB}$ of $Ni(OH)_2$ is –1.31 V[52]. By combining the band gap ($E_g$) of the catalyst in Figure S3 and $E_{VB} = E_{CB} + E_g$, the $E_{VB}$ potentials of $CeO_2$ and $Ni(OH)_2$ are 2.14 and 1 V, respectively.

**Photocatalytic Mechanism.** Based on the above experimental conclusions, Figure 5 shows the possible photo-induced electrons transfer paths in the composite catalyst. Under the irradiation of visible light, the valence electron on EY transfers from HOMO to the LOMO orbital. EY has a more negative energy level, which facilitates the transfer of electrons to the semiconductor catalyst. The electrons in the valence band of $CeO_2$ are excited to the conduction band and then transfer to $Ni_2P$, while the holes on the VB are consumed by TEOA. EY and $CeO_2$ are the main electron donors, and $Ni_2P$ with lower reduction potential is the main hydrogen evolution site, which is the final flow direction of photogenerated electrons. The reaction process of dye molecules has been described in detail in the previous article.[53]

In terms of morphology control, $Ni(OH)_2$ nanoflowers are phosphated at high temperature to form small-sized $Ni_2P$ simple flower-like clusters of nanoplates. Nanoflower, nanoplates and interlayer gaps provide a broad place for anchoring $CeO_2$ nanoparticles. The staggered energy band structure of NHC-15 is conducive to the separation of electrons and holes, and it has similar morphological advantages to NPC-15. The unique 3D/0D structure of the two composite catalysts makes the nanoparticles have good dispersibility and shortens the electron transmission path.

## n CONCLUSION

$Ni(OH)_2$ and $Ni_2P$ modified $CeO_2$ photocatalyst greatly improve the performance of photocatalytic hydrogen production. The hydrogen evolution of NPC-15 under visible light irradiation was

  
DOI: 10.14102/j.cnki.0254-5861.2021-0057

12 times that of NHC-15. Mechanism studies have shown that $Ni_2P$ is not only the main hydrogen evolution site, but also broadens the optical region for light harvesting of the catalyst, revealing the role of the 3D/0D structure in inhibiting nanoparticle agglomeration and shortening the electron capture and transport distance. This research provides new ideas for the rational design of composite catalyst structure and the introduction of co-catalysts to improve performance.

## n EXPERIMENTAL

**Material Preparation.** The preparation steps of $CeO_2$ nanoparticles:[32] 1.75 g $Ce(NO_3)_3·6H_2O$ was added to deionized water (80 mL) and stirred for 5 min, followed by adding 1.65 g NaOH and vigorous stirring for 1 h. The mixed liquid was poured to a Teflon-lined autoclave and reacted at 180 ºC for 12 h. After that, the reaction solution was centrifuged (9000 rpm, 3 min) for several times with water and alcohol, providing the final light yellow solid to be $CeO_2$ nanoparticles.

$Ni(OH)_2$ nanoflowers were prepared based on previous reports.[54] 12 mmol $CH_4N_2O$, 6 mmol $NH_4F$, and 1 mmol $NiCl_2·6H_2O$ were dissolved in deionized water (54 mL) and stirred or 1 h. The mixed solution was poured into an autoclave and reacted at 180 ºC for 12 h. $Ni(OH)_2$ nanoflowers were obtained by multiple centrifugal washing with alcohol and water. The mass ratio of $NaH_2PO_2$ and $Ni(OH)_2$ is 3:1, and the two samples were ground and placed in a magnetic boat and reacted at 300 °C under $N_2$ for 2 h with a ramp rate of 3 ºC/min. The subsequent processing steps were the same as $CeO_2$, and the final product was $Ni_2P$.

The 5, 10, 15, 20 and 25 mg of $Ni_2P$ and 0.1 g of $CeO_2$ were added to 60 mL of alcohol solution, heated and rotated in a water bath at 60 °C until it was dried, obtaining the composite catalyst called NPC-x. According to the same method by using 15 mg $Ni(OH)_2$ and 0.1 g $CeO_2$, the material thus obtained is named NHC-15.

**Characterization.** X-ray diffraction (XRD) patterns recorded the crystallinity of samples in the range of 5° to 80° on Rigaku RINT-2000 adopting CuKα radiation. The microstructures of the catalysts were characterized by transmission electron microscope (TEM: JEM-2100F, JEOL) and scanning electron microscopy (SEM: EVO 10 ZEISS). Referred to $BaSO_4$, ultraviolet-visible diffuse reflectance spectra (UV-vis DRS: PerkinElmer Lamda-750) were used to study the absorption characteristics of the catalysts. The X-ray photoelectron spectroscopy (XPS: Thermo Scientific ESCALAB $Xi^+$) was used to study the element valence states of catalysts. Brunauer-Emmett-Teller (BET) and pore size distribution of samples were measured on an ASAP 2460. Photoluminescence (PL: FluoroMax-4, HORIBA) and time-resolved photoluminescence (TRPL: Fluorohub-B, HORIBA) tested the photochemical properties of the catalyst. The electrochemical experiment of the catalyst was carried out on the electrochemical workstation (VersaSTAT4-400, AMETEK), in which the electrolyte was $NaSO_4$ electrolyte (0.2 M) and the light source was 300W Xenon lamp (Microsolar300, Bejing Perfectlight).

**Photocatalytic Activity Experiments.** In a 63 mL sealed quartz bottle, 10 mg EY and 10 mg samples were dissolved in a TEOA solution (30 mL, 15% v/v mL). The quartz bottle was filled with $N_2$ to replace other gases, and the hydrogen production experiment of the catalyst was tested in a multi-channel photochemical reaction system (PCX-50B, Beijing Perfectlight). The gas chromatography (Tianmei GC7900) was used to analyze the hydrogen content in the quartz bottles.

## n ACKNOWLEDGEMENTS

This work was financially supported by the Chinese National Natural Science Foundation (201862002).

## n AUTHOR CONTRIBUTIONS

Teng Yan and Hua Liu conceived and designed the experiments; Teng Yan and Zhiliang Jin performed the experiments; Zhiliang Jin and Xiaojie Zhang contributed reagents/materials and analysis tools; and Teng Yan wrote the paper.

## n AUTHOR INFORMATION

Corresponding author. zl-jin@nun.edu.cn (Z. L. Jin)

## n COMPETING INTERESTS

The authors declare that they have no competing interests.

## n ADDITIONAL INFORMATION

Supplementary information is available for this paper at http://manu30.magtech.com.cn/jghx/EN/10.14102/j.cnki.0254-5861.2021-0057

For submission: https://mc03.manuscriptcentral.com/cjsc

## n REFERENCES

(1) Li, Y. X.; Zhang, W. Z.; Li, H.; Yang, T. Y.; Peng, S. Q.; Kao, C.; Zhang, W. Y. Ni–B coupled with borate-intercalated $Ni(OH)_2$ for efficient and stable electrocatalytic and photocatalytic hydrogen evolution under low alkalinity. *Chem. Eng. J.* **2020**, 394, 124928.

(2) Cai, H.; Han, D. Y.; Wang, X. N.; Cheng, X. X.; Liu, J.; Jia, L.; Ding, Y.; Liu, S. X.; Fan, X. X. High specific surface area defective g-$C_3N_4$ nanosheets with enhanced photocatalytic activity prepared by using glyoxylic acid mediated melamine. *Mater. Chem. Phys.* **2020**, 256, 123755.

(3) Wu, H. S.; Miao, T. F.; Shi, H. X.; Xu, Y.; Fu, X. L.; Qian, Li. Probing photocatalytic hydrogen evolution of cobalt complexes: experimental and theoretical methods. *Chin. J. Struct. Chem.* **2021**, 40, 1696–1709.

(4) Li, X. F.; Wu, X. F.; Liu, S. W.; Li, Y. H.; Fan, J. J.; Lv, K. L. Effects of fluorine on photocatalysis. *Chin. J. Catal.* **2020**, 41, 1451–1467.

(5) Sun, G. T.; Xiao, B.; Shi, J. W.; Mao, S. M.; He C.; Ma D. D.; Cheng Y. H. Hydrogen spillover effect induced by ascorbic acid in CdS/NiO core-shell p–n heterojunction for significantly enhanced photocatalytic $H_2$ evolution. *J. Colloid Interface Sci.* **2021**, 596, 215–224.

(6) Lin, X.; Du, S. W.; Li, C. H.; Li, G. J.; Li, Y. J.; Chen, F. T.; Fang, P. F. Consciously constructing the robust NiS/g-$C_3N_4$ hybrids for enhanced photocatalytic hydrogen evolution. *Catal. Lett.* **2020**, 7, 1898–1908.

(7) Wang, P.; Yang, M.; Tang, S. P.; Chen, F. T.; Li, Y. J. Preparation of cellular $C_3N_4$/$CoSe_2$/GA composite photocatalyst and its $CO_2$ reduction activity. *Chem. J. Chinese U.* **2021**, 6, 1924–1932.

(8) Yu, J. G.; Li, X.; Ong, W. J.; Zhang, L. Y. Design and fabrication of advanced photocatalysts. *Acta Phys.-Chim. Sin.* **2021**, 37, 2012043.

(9) Lai, L. J.; Xing, F. S.; Cheng, C. C.; Huang, C. J. Hierarchical 0D $NiSe_2$/2D $ZnIn_2S_4$ nanosheet-assembled microflowers for enhanced photocatalytic hydrogen evolution. *Adv. Mater. Interfaces.* **2021**, 8, 2100052.

(10) Zhang, M. D.; Yi, J. D.; Huang, Y. B.; Cao, R. Covalent triazine

  
DOI: 10.14102/j.cnki.0254-5861.2021-0057

frameworks-derived N, P dual-doped porous carbons for highly efficient electrochemical reduction of $CO_2$. *Chin. J. Struct. Chem.* **2021**, 9, 1213–1222.

(11) Tang, N. M.; Li, Y. J.; Chen, F. T.; Han, Z. Y. In situ fabrication of a direct Z-scheme photocatalyst by immobilizing CdS quantum dots in the channels of graphene-hybridized and supported mesoporous titanium nanocrystals for high photocatalytic performance under visible light. *Rsc. Adv.* **2018**, 73, 42233–42245.

(12) Li, Y.; Zhang, D. N.; Fan, J. J.; Xiang, Q. J. Highly crystalline carbon nitride hollow spheres with enhanced photocatalytic performance. *Chin. J. Catal.* **2021**, 42, 627–636.

(13) Li, F.; Cheng, L.; Xiang, Q. J. Steering the behavior of photogenerated carriers in semiconductor photocatalysts: a new insight and perspective. *J. Mater. Chem. A* **2021**, 9, 23765–23782.

(14) Liu, H.; Yan, T.; Jin, Z. L.; Ma, Q. X. CoP nanoparticles as cocatalyst modified the CdS/$NiWO_4$ p–n heterojunction to produce hydrogen efficiently. *New J. Chem.* **2020**, 44, 1426–1438.

(15) Cao, D.; An, H.; Yan, X. Q.; Zhao, Y. X.; Yang, G. D.; Mei, H. Fabrication of Z-scheme heterojunction of SiC/Pt/Cds nanorod for efficient photocatalytic $H_2$ evolution. *Acta Phys.-Chim. Sin.* **2020**, 36, 1901051.

(16) Zhang, J. W.; Cheng, C. C.; Xing, F. S.; Cheng, C.; Huang, C. J. 0D *β*-$Ni(OH)_2$ nanoparticles/1D $Mn_{0.3}Cd_{0.7}S$ nanorods with rich S vacancies for improved photocatalytic $H_2$ production. *Chem. Eng. J.* **2021**, 414, 129157.

(17) Zhang, M. Y.; Nie, S. Y.; Cheng, T.; Feng, Y.; Zhang, C. C.; Zheng, L.; Wu, L.; Hao, W. C.; Ding, Y. Enhancing the macroscopic polarization of CdS for piezo-photocatalytic water splitting. *Nano Energy* **2021**, 90, 106635.

(18) Yang, H.; Zhang, J. F.; Dai, K. Organic amine surface modified 1D $CdSe_{0.8}S_{0.2}$-DETA/2D $SnNb_2O_6$ S-scheme heterojunction with promoted visible-light-driven photocatalytic $CO_2$ reduction. *Chin. J. Catal.* **2022**, 43, 255–264.

(19) Shen, R.; Ren, D.; Ding, Y.; Guan, Y.; Ng, Y. H.; Zhang, P.; Li, X. Nanostructured CdS for efficient photocatalytic $H_2$ evolution: a review. *Sci. China Mater.* **2020**, 63, 2153–2188.

(20) Chen, X.; Ke, X. C.; Zhang, J. F.; Yang, C. C.; Dai, K.; Liang, C. H. Insight into the synergy of amine-modified S-scheme $Cd_{0.5}Zn_{0.5}Se$/porous g-$C_3N_4$ and noble-metal-free $Ni_2P$ for boosting photocatalytic hydrogen generation. *Ceram. Int.* **2021**, 47, 13488–13499.

(21) Liu, J. F.; Wang, P.; Fan, J. J.; Yu, H. G.; Yu, J. G. In situ synthesis of $Mo_2C$ nanoparticles on graphene nanosheets for enhanced photocatalytic $H_2$-production activity of $TiO_2$. *ACS Sustainable Chem. Eng.* **2021**, 9, 3828–3837.

(22) Shen, R.; Ding, Y.; Li, S.; Zhang, P.; Xiang, Q.; Ng, Y. H.; Li, X. Constructing low-cost $Ni_3C$/twin-crystal $Zn_{0.5}Cd_{0.5}S$ heterojunction/homojunction nanohybrids for efficient photocatalytic $H_2$ evolution. *Chin. J. Catal.* **2021**, 42, 25–36.

(23) Jiang, Z.; Chen, Q.; Zheng, Q.; Shen, R.; Zhang, P.; Li, X. Constructing 1D/2D schottky-based heterojunctions between $Mn_{0.2}Cd_{0.8}S$ nanorods and $Ti_3C_2$ nanosheets for boosted photocatalytic $H_2$ evolution. *Acta Phys.-Chim. Sin.* **2021**, 37, 2010059.

(24) Sun, G. T.; Xiao, B.; Zheng, H.; Shi, J. W.; Mao, S. M.; He, C.; Li, Z. H.; Cheng, Y. H. Ascorbic acid functionalized CdS-ZnO core-shell nanorods with hydrogen spillover for greatly enhanced photocatalytic $H_2$ evolution and outstanding photostability. *J. Mater. Chem. A* **2021**, 9, 9735–9744.

(25) Ma, D. D.; Shi, J. W.; Sun, D. K.; Zou, Y. J.; Cheng, L. H.; He, C.; Wang, H. K.; Niu, C. M.; Wang, L. Z. Au decorated hollow ZnO@ZnS heterostructure for enhanced photocatalytic hydrogen evolution: the insight into the roles of hollow channel and Au nanoparticles. *Appl. Catal. B Environ.* **2019**, 244, 748–757.

(26) Cao, R. Y.; Yang, H. C.; Zhang, S. W.; Xu, X. J. Engineering of Z-scheme 2D/3D architectures with $Ni(OH)_2$ on 3D porous g-$C_3N_4$ for efficiently photocatalytic $H_2$ evolution. *Appl. Catal. B Environ.* **2019**, 258, 117997.

(27) Ma, D. D.; Shi, J. W.; Sun, L. W.; Sun, Y. X.; Mao, S. M.; Pu, Z. X.; He, C.; Zhang, Y. J.; He, D.; Wang, H. K.; Cheng, Y. H. Knack behind the high performance CdS/ZnS-NiS nanocomposites: optimizing synergistic effect between cocatalyst and heterostructure for boosting hydrogen evolution. *Chem. Eng. J.* doi.org/10.1016/j.cej.2021.133446.

(28) You, Z. Y.; Liao, Y. L.; Li, X.; Fan, J. J.; Xiang, Q. J. State-of-the-art recent progress in MXene-based photocatalysts: a comprehensive review. *Nanoscale*. **2021**, 13, 9463–9504.

(29) Li, Y.; Li, X.; Zhang, H. W.; Fan, J. J.; Xiang, Q. J. Design and application of active sites in g-$C_3N_4$-based photocatalysts. *J. Mater. Sci. Technol.* **2020**, 56, 69–88.

(30) Wen. P.; Zhao, K. F.; Li, H.; Li, J. S.; Li, J.; Ma, Q; Geyer, S. M.; Jiang, L.; Qiu, Y. J. In situ decorated $Ni_2P$ nanocrystal co-catalysts on g-$C_3N_4$ for efficient and stable photocatalytic hydrogen evolution via a facile co-heating method. *J. Mater. Chem. A* **2020**, 8, 2995–3004.

(31) Shi, J. W.; Zou, Y. J.; Cheng, L. H.; Ma, D. D.; Sun, D. K.; Mao, S. M.; Sun, L. W.; He, C.; Wang, Z. Y. In-situ phosphating to synthesize $Ni_2P$ decorated NiO/g-$C_3N_4$ p-n junction for enhanced photocatalytic hydrogen production. *Chem. Eng. J.* **2019**, 378, 122161.

(32) Mohanty, B.; Chattopadhyay, A.; Nayak, J. Band gap engineering and enhancement of electrical conductivity in hydrothermally synthesized $CeO_2$-PbS nanocomposites for solar cell applications. *J. Alloys Compd.* **2021**, 850, 156735.

(33) Li, P.; Zhou, Y.; Zhao, Z. Y.; Xu, Q. F.; Wang, X. Y.; Xiao, M.; Zou, Z. G. Hexahedron prism-anchored octahedronal $CeO_2$: crystal facet based homojunction promoting efficient solar fuel synthesis. *J. Am. Chem. Soc.* **2015**, 13, 79547–9550.

(34) Wang, D.; Yin, F. X.; Cheng, B.; Xia, Y.; Yu, J. G.; Ho, W. K. Enhanced photocatalytic activity and mechanism of $CeO_2$ hollow spheres for tetracycline degradation. *Rare Met.* **2021**, 40, 2369–2380.

(35) Ma, Y. J.; Bian, Y.; Liu, Y.; Zhu, A. Q.; Wu, H.; Cui, H.; Chu, D. W.; Pan J. Construction of Z-scheme system for enhanced photocatalytic $H_2$ evolution based on CdS quantum dots/$CeO_2$ nanorods heterojunction. *ACS Sustainable Chem. Eng.* **2017**, 6, 2552–2562.

(36) Ma, Y. J.; Ou, P. F.; Wang, Z. Y.; Zhu, A. Q.; Lu, L. L.; Zhang, Y. H.; Zeng, W. X.; Song, J.; Pan, J. Interface engineering in $CeO_2$ (111) facets decorated with CdSe quantum dots for photocatalytic hydrogen evolution. *J. Colloid Interface Sci.* **2020**, 579, 707–713.

(37) Suman.; Singh, S.; Ankita.; Kumar, A.; Kataria, N.; Kumar, S.; Kumar, P. Photocatalytic activity of α-$Fe_2O_3$@$CeO_2$ and $CeO_2$@α-$Fe_2O_3$ core-shell nanoparticles for degradation of Rose Bengal dye. *J. Environ. Chem. Eng.* **2021**, 9, 106266.

(38) Zou, W. X.; Shao, Y.; Pu, Y.; Luo, Y. D.; Sun, J. F.; Ma, K. L.; Tang, C. J.; Gao, F.; Dong, L. Enhanced visible light photocatalytic hydrogen evolution via cubic $CeO_2$ hybridized g-$C_3N_4$ composite. *Appl. Catal. B Environ.* **2017**, 218, 51–59.

(39) Li, P. Y.; Hong, W. T.; Liu, W. Fabrication of large scale self-supported WC/$Ni(OH)_2$ electrode for high-current-density hydrogen evolution. *Chin. J. Struct. Chem.* **2021**, 40, 1365–1371.

(40) Wang, Q.; Liu, Z. Q.; Zhao, H. Y.; Huang, H.; Jiao, H.; Du, Y. P. MOF-derived porous $Ni_2P$ nanosheets as novel bifunctional electrocatalysts for the hydrogen and oxygen evolution reactions. *J. Mater. Chem. A* **2018**, 6, 18720–18727.

  
DOI: 10.14102/j.cnki.0254-5861.2021-0057

(41) Dong, B.; Li, L. Y.; Dong, Z. F.; Xu, R.; Wu, Y. Fabrication of $CeO_2$ nanorods for enhanced solar photocatalysts. *Int. J. Hydrogen Energy* **2018**, 43, 5275–5282.

(42) Luo, X.; Li, R.; Homewood, K. P.; Chen, X. X.; Gao, Y. Hybrid 0D/2D $Ni_2P$ quantum dot loaded $TiO_2$(B) nanosheet photothermal catalysts for enhanced hydrogen evolution. *Appl. Surf. Sci.* **2020**, 505, 144099.

(43) Liu, Y. R.; Hu, W. H.; Li, X.; Dong, B.; Shang, X.; Han, G. Q.; Chai, Y. M.; Liu, Y. Q.; Liu, C. G. One-pot synthesis of hierarchical $Ni_2P/MoS_2$ hybrid electrocatalysts with enhanced activity for hydrogen evolution reaction. *Appl. Surf. Sci.* **2016**, 383, 276–282.

(44) Li, T.; Jin, Z. L. Unique ternary Ni-MOF-74/$Ni_2P/MoS_x$ composite for efficient photocatalytic hydrogen production: role of $Ni_2P$ for accelerating separation of photogenerated carriers. *J. Colloid Interface Sci.* **2022**, 605, 385–397.

(45) Li, T.; Wang, X. F.; Jin, Z. L. MoC quantum dots modified by $CeO_2$ dispersed in ultra-thin carbon films for efficient photocatalytic hydrogen evolution. *Mol. Catal.* **2021**, 513, 111829.

(46) Yan, T.; Liu H.; Jin, Z. J. Graphdiyne based ternary GD-CuI-$NiTiO_3$ S-scheme heterjunction photocatalystfor hydrogen evolution. *ACS Appl. Mater. Interfaces* **2021**, 13, 24896–24906.

(47) Li, D. J.; Ma, X. L.; Su, P.; Yang, S. J.; Jiang, Z. B.; Li, Y. J.; Jin, Z. J. Effect of phosphating on NiAl-LDH layered double hydroxide form S-scheme heterojunction for photocatalytic hydrogen evolution. *Mol. Catal.* **2021**, 516, 111990.

(48) Wang, Y. P.; Hao, X. Q.; Zhang, L. J.; Jin, Z. L.; Zhao T. S. Amorphous $Co_3S_4$ nanoparticle-modified tubular g-$C_3N_4$ forms step-scheme heterojunctions for photocatalytic hydrogen production. *Catal. Sci. Technol.* **2021**, 11, 943.

(49) Li, H. J.; Gao, Y. Y.; Zhou, Y.; Fan, F. T.; Han, Q. T.; Xu, Q. F.; Wang, X. Y.; Xiao, M.; Li, C.; Zou, Z. G. Construction and nanoscale detection of interfacial charge transfer of elegant Z-scheme $WO_3$/Au/$In_2S_3$ nanowire arrays. *Nano Lett.* **2016**, 16, 5547–5552.

(50) Meng, X. B.; Sheng, J. L.; Tang, H. L.; Sun, X. J.; Dong, H.; Zhang, F. M. Metal-organic framework as nanoreactors to co-incorporate carbon nanodots and CdS quantum dots into the pores for improved $H_2$ evolution without noble-metal cocatalyst. *Appl. Catal. B Environ.* **2019**, 244, 340–346.

(51) Bie, C. B.; Yu, H. G.; Cheng, B.; Ho, W. K.; Fan, J. J.; Yu, J. G. Design, fabrication, and mechanism of nitrogen-doped graphene-based photocatalyst. *Adv. Mater.* **2021**, 33, 2003521.

(52) Liu, Y.; Sun, Y. P.; Xu, J.; Mao, M.; Li, X. H. A Z-scheme heterostructure constructed from ZnS nanospheres and $Ni(OH)_2$ nanosheets to enhance the photocatalytic hydrogen evolution. *New J. Chem.* **2021**, 45, 7781.

(53) Yan, T.; Liu, H.; Jin, Z. L. g-$C_3N_4$/α-$Fe_2O_3$ supported zero-dimensional $Co_3S_4$ nanoparticles form S-scheme heterojunction photocatalyst for efficient hydrogen production. *Energy Fuels.* **2021**, 35, 856–867.

(54) Liu, Y.; Xu, J.; Ding, Z. F.; Mao, M.; Li, L. J. Marigold shaped mesoporous composites $Bi_2S_3/Ni(OH)_2$ with n–n heterojunction for high efficiency photocatalytic hydrogen production from water decomposition. *Chem. Phys. Lett.* **2021**, 766, 138337.

Received: December 16, 2021
Accepted: January 6, 2022
Published: January 13, 2022

  
DOI: 10.14102/j.cnki.0254-5861.2021-0057